
Article:
Wolde, S, Lao, YF, Pitigala, PKDDP et al. (4 more authors) (2016) Low-frequency noise properties of p-type GaAs/AlGaAs heterojunction detectors. Infrared Physics and Technology, 78. pp. 99-104. ISSN 1350-4495

https://doi.org/10.1016/j.infrared.2016.07.018

Low-frequency noise properties of *p*-type GaAs/AlGaAs heterojunction detectors

Seyoum Wolde[1], Y. F. Lao[1], P. K. D. D. P. Pitigala[1], A. G. U. Perera[1*], L. H. Li[2], S. P. Khanna[2**], E. H. Linfield[2]

[1]*Department of Physics and Astronomy, Georgia State University, Atlanta, GA 30303, USA.*

[2]*The School of Electronic and Electrical Engineering, University of Leeds, Leeds LS2 9JT, UK.*

Abstract

We have measured and analyzed, at different temperatures and bias voltages, the dark noise spectra of GaAs/AlGaAs heterojunction infrared photodetectors, where a highly doped GaAs emitter is sandwiched between two AlGaAs barriers. The noise and gain mechanisms associated with the carrier transport are investigated, and it is shown that a lower noise spectral density is observed for a device with a flat barrier, and thicker emitter. Despite the lower noise power spectral density of flat barrier device, comparison of the dark and photocurrent noise gain between flat and graded barrier samples confirmed that the escape probability of carriers (or detectivity) is enhanced by grading the barrier. The grading suppresses recombination owing to the higher momentum of carriers in the barrier. Optimizing the emitter thickness of the graded barrier to enhance the absorption efficiency, and increase the escape probability and lower the dark current, enhances the specific detectivity of devices.

Key words: Graded barrier, Noise, AlGaAs, GaAs, Gain.

[*] Corresponding author email: uperera@phy-astr.gsu.edu

[**]Current address: Physics of Energy Harvesting, CSIR-National Physical Laboratory, New Delhi, India.

I. Introduction

Understanding the physical origins and mechanisms responsible for different types of electronic noise is important in optimizing the performance of a broad range of electronic devices. Electronic noise can originate from dark currents, temperature fluctuations, and trap states. The fundamental noise components (shot noise and thermal noise), are frequency independent, and can be controlled to some extent by the choice of device architecture, and through optimizing the detailed design[1], including the choice of active materials, growth technique, operating temperature, and doping levels.

The presence of defects and impurities results in large fluctuations in electronic conductivity through fluctuations of carrier density,[2] mobility[3] or a combination of the two[4-6]. The net charge of any defect is then determined by the emission and capture of carriers. A defect trap is charged upon carrier emission, and neutralized upon carrier capture. These fluctuations in carrier numbers due to trapping, and in some cases phonon scattering, lead to generation-recombination (G-R) noise. Studies of hole traps in unintentionally *p*-type doped GaAs layers have been investigated previously,[7] together with the low-frequency noise properties of beryllium-doped GaAs/AlAs[1] quantum well and epitaxial layers of $Al_{0.5}Ga_{0.5}As$[8] grown by molecular beam epitaxy (MBE).

In this article, we investigate *p*-type beryllium-doped infrared photodetectors in which a GaAs emitter is sandwiched between undoped AlGaAs barriers. Having a doped emitter can lead to excess noise owing to traps formed by ionized clustering of impurities,[9] and this can reduce the gain of optoelectronic devices. This G-R noise has the general property that the noise spectral density increases at lower frequencies and so low-frequency noise (LFN) measurement can be utilized as a diagnostic tool to characterize devices[10]. The aim of our present study is to characterize the various contributions of noise on the performance of an infrared photodetector, and specifically their effect on device gain. We investigate the noise and gain mechanisms associated with carrier transport for different barriers and emitter thicknesses in terms of a range of parameters used for optimizing the detectivity of devices, including the dark current, photo-absorption, and capture probability.

II. Device structures and experimental procedures

Four detector designs were investigated (Table 1), with the valence band profile of the structures being shown in Figure 1. All structures have a highly *p*-doped ($1x10^{19}$ cm^{-3}) emitter sandwiched between two undoped AlGaAs barriers. In three of the structures, one of the barriers is graded, whilst in the fourth structure, both barriers have a constant height. The width of the graded barrier is 80 nm in SP1005, SP1006 and SP1007, and the aluminum mole fraction is changed uniformly from 0.45 (X_1) to

0.75 (X_2) by adjusting the cell temperatures during growth to give a "continuous" (also known as "averaging") approach to the grading. The side of the barrier with the lower aluminum mole fraction (X_1) is next to the bottom contact. A second barrier with a constant 0.57 (X_3) aluminum mole fraction then separates the emitter from the top contact, and has a width of 400 nm. SP1005, SP1006, and SP1007 differ from each other by the emitter thickness. In SP1001, both barriers have a constant height: the first barrier has a mole fraction of 0.75 ($X_1 = X_2$), and the second barrier 0.57 (X_3). For all devices, photo-absorption in the emitter excites carriers from the light/heavy hole bands into the split-off band. The excited carriers then escape from the emitter layer after scattering out of split-off band back into the light/heavy hole band at the emitter-barrier interface[11] as shown in Figure 1. Detailed explanations of detection mechanism, as well as details of the growth of all structures, have been reported previously in Pitigala, et al[11, 12].

In order to determine the low frequency noise, devices were biased with a DC voltage source. The voltage and current noise spectra were then amplified using a Stanford Research System SR560 low-noise voltage amplifier with a fixed gain of G = 1000 and an SR 570 low-noise current preamplifier, respectively, and measured using an HP SRS-SR785 spectrum analyzer in a frequency range of 1 Hz-102 kHz. Devices were mounted on a holder placed on the cold head of a liquid nitrogen-cooled dewar, and the temperature was measured using a 330 Lake Shore controller. The detector, amplifier, and dry battery providing the bias voltage were shielded in a grounded aluminum box to prevent the external environment influencing the background noise. The input voltage noise of the apparatus was determined by shorting out the sample; and was found to be independent of temperature. The noise power spectral density was then measured in three to four different overlapping frequency spans. At low frequencies, the small bin width of 0.125 Hz is used to ensure better frequency resolution and accuracy of the measurements.

III. Results and discussion

The four most common noise components are thermal, shot, G-R, and 1/f. Thermal noise is due to thermal motion of carriers and is given by $S_{th} = 4KT/R,$ where T is the temperature and R is the resistance of the device, and this noise mechanism is frequency independent. Shot noise is also frequency independent, and originates from the discrete nature of carriers; its power spectral density is given by $S_{sh} = 2eI,$ where I is the current supplied by the DC source. Defects, impurities, and band discontinuities can, however, trap carriers, interrupting the current flow. If the trap levels are all identical, then there is a continuous emission and capture of holes between the traps and the valence

band. Hence, the number of trapped and free carriers will fluctuate with the generation-recombination spectrum of the carriers due to these fluctuations being given by:[13, 14]

$$S_n(f) = \langle(\Delta n)^2\rangle \frac{4\tau}{1+(2\pi f\tau)^2}, \quad (1)$$

where $\langle(\Delta n)^2\rangle$ is the variance of the number of trapped carriers, f is frequency and τ is the characteristic time. At a given temperature, the maximum G-R noise level is observed when $2\pi f\tau = 1$. Superposition of many G-R processes with a smooth distribution of characteristic times then leads to a 1/f noise spectrum[1], where the intensity is proportional to the number of trap centers.

The origin of $1/f$ noise is generally explained by two models: noise related to mobility fluctuations$(\Delta\mu)$, and noise related to carrier density fluctuations (ΔN). However, the conductance, or resistance *R,* of a semiconductor also fluctuates with a l/f spectrum[13]. The conductance fluctuations of an ohmic sample can be measured as voltage fluctuations when a constant current *I* is passed through the sample, or as current fluctuations when the voltage drop *V* across the sample is kept constant. The low-frequency $1/f$ noise behavior is expressed simply by the equation[13]:

$$\frac{S_R(f)}{R^2} = \frac{S_I(f)}{I^2} = \frac{S_V(f)}{V^2} = \frac{A_{1/f}}{f}, \quad (2)$$

where $A_{1/f}$ is a measure of the relative amplitude of the noise of the sample, and $S_R(f)$, $S_V(f)$, and $S_I(f)$ are the noise power spectral densities of resistance, voltage, and current, respectively. The G-R noise (equation (1)) may be associated with multiple trap levels of different relaxation times τ_i, which are assumed to be uncorrelated, and hence the corresponding terms can be added. The total noise power spectral density is a combination of 1/f noise, G-R noise, thermal noise, and shot noise, and can be described by the equation:[13]

$$S(f,T) = \frac{A(T)I^2}{f^\alpha} + \sum_{i=1}^{n} \frac{B(T)\tau_i}{1+(2\pi f\tau_i)^2} + S_{white} \quad (3)$$

where α is the frequency exponent in $S(f) \propto 1/f^\alpha$, and S_{white} can be either thermal, shot or a combination of these noise mechanisms. The second expression on the right hand side of equation (3) represents the noise power spectral density of the G-R term resulting from a sum of *n* distinct trap levels. *A (T)* and *B (T)* are parameters related to the amplitude of *1/f* and G-R noise at a particular temperature, respectively.

Figure 2 shows that, at low temperatures ($\approx 78\,K$), and low biases ($-1\,V < V$ (bias) $< 0\,V$ with the negative bias applied to the top contact, or $0\,V < V$ (bias) $< \sim 6.2\,V$ in the positive bias), the dark current is low, below $8\text{x}10^{-11}$ A. At higher biases, however, both the dark current and its noise increase. At low bias voltages and temperatures, the device stays predominantly in the high resistivity state where the noise current is low and independent of frequency. The noise current calculated from the measured

dark current and differential resistance of these devices is then dominated by noise resulting from the DC current supplied, with negligible contribution from thermal excitations. 1/f, shot, and G-R noises are all, however, current dependent. Since high resistance at low temperature is characterized by very small numbers of activated carriers in the device, 1/f noise for low DC current is not expected. But, the dominant source of G-R noise is trap and defect sites, creating fluctuations in the carrier density throughout the detector. Experimental result reveals[15] that the noise power densities of these devices are dominated by G-R noise at lower bias and lower temperatures. The power spectral density of G-R noise has a Lorentzian form. However, at low frequencies, the plateau of Lorentzian power spectral density[16] has the form $S_n(f) = 4qI_d g_n \Delta f$, which is frequency independent, up to a cutoff frequency located in the GHz range, above which the noise power spectral density rolls down as $1/f^2$.

Figure 3 shows that the noise spectral density, S (*f*) at 120 K under different bias voltages for sample SP1005. At lower bias, i.e. higher resistance, the dominant noise is G-R, and hence the noise spectral density is independent of frequency. As the temperature increases from 78 K to 300 K (Figure 2) and/or the bias voltage increases (Figure 3), however, the system steadily switches to the low resistivity state, leading to other components of noise being observed, including 1/f noise with a bias dependent cut off frequency ranging from ~10 to ~1000 Hz (Figure 3), and Johnson noise[1].

The dark current-voltage, IV, characteristics of the devices at liquid nitrogen and room temperatures are shown in Figure 2. The asymmetry in the IV trace is due to the asymmetry in the structure caused by both the graded barrier, and also the different heights and widths of the upper and lower barriers. The device SP1001 (which has a constant barrier) has the lowest dark current. The higher dark current in the graded barrier structure under negative bias can be explained by referring to the energy band alignments under applied electric field (Figure 4).Under negative bias, the valence band (VB) energy of the bottom contact will move down, making the graded barrier more flat, and hence the effective barrier height will be lowered. Therefore, a higher dark current can be expected compared to the constant barrier structure. At low positive bias, a charge build up in the graded barrier structures will lower the valence band energy at the bottom contact, compared to the fixed barrier height sample, and hence, once again, cause a higher dark current. Furthermore, given the constant barrier sample (SP1001) has a larger percentage of aluminum compared to other SP100X series samples, where the graded barriers have an average mole fraction of ~ 0.60, SP1001 has the highest resistance, supporting the experimental observation of lower noise levels.

In Figure 5 (a), it can clearly be seen that the noise power spectral density, S (*f*), of SP1001 is lower than in the graded barrier structures. In all cases, the noise power spectral density increases with

(negative) bias voltage and temperature owing to a decreasing dynamic resistance of the device as illustrated in Figures 5 (b) and 6, respectively, for SP1005. It is also found that all devices have higher noise power spectral density for negative biases (inset of Figure 5 (b)). Figure 5 (b) shows, for bias voltages higher than - 0.4 V and frequencies higher than ~10 kHz, that the device exhibits white noise spectra that are very close to the noise level of the measurement system, and hence it is difficult to see a bias dependence. However, at room temperature, based on the noise power spectral density measured at - 0.2 V, and its calculated fit, the device exhibits the four types of noises: 1/f, G-R, shot, and thermal noise (Figure 7). In the region, where the excess noise ($1/f^{\alpha}$ and G-R) is dominant (Figure 5 (b)), α is found to be 1 ± 0.1 at a bias voltage of - 50 mV. As the bias increased, α then varied from 1.0 to 1.5. No significant differences were, however, observed in spectral noise density for different emitter thicknesses (Figure 8 (a)).

One can assume that dark current and background photon noise limit the performance of photoconductive detectors. In the dark current limited condition, fluctuation in the number of mobile carriers via trapping and escape processes control the dark current, and the noise associated with the dark current is G-R in nature. The noise current I_n in the device is, therefore, related to the corresponding dark current I_d by:[16]

$$I_n^2 = 4qI_d g_n \Delta f, \tag{4}$$

where g_n is the noise gain and Δf is the bandwidth of the measurement. According to Liu[16], the expressions for noise current gain, g_n, and photocurrent gain, g_p, are given by:

$$g_n = \frac{1}{Np_c} \text{ and } g_p = \frac{1-p_c}{Np_c}, \tag{5}$$

respectively, where p_c is the capture probability of carriers traversing an emitter and N is the total number of emitters. If the capture probability $(p_c) \ll 1$, the difference between the noise current gain and photocurrent gain may be ignored and they are both given by $1/Np_c$. If we neglect tunneling, the capture probability for transport of carriers associated with dark current and photoelectrons are the same, i.e. except for the emission mechanism; both dark current and photocurrent follow the same path. For a detector in the background limited performance (BLIP) condition, the intrinsic noise of the detector is negligible compared to the noise due to the fluctuation of the number of incident background photons. As a result, the total noise is determined by the photocurrent under background illumination. Hence, the detector noise associated with background radiation is given by:[17, 18]

$$I_{Bn}^2 = 4q g_n I_p \Delta f, \tag{6}$$

where the total current in background limited operation is given by $I_p = e\eta g_p \phi_B$ (where ϕ_B is the incident photon flux and η is the total photoionization efficiency). The dark current can be written

as$I_{dark} = g_n i_{em}$, where i_{em} is the thermal emission current from the structure. The specific detectivity, $D^* = R\sqrt{A\Delta f}/I_n$, where R is the responsivity and A is the area of the device. If the detectivity is normalized by the detector area and bandwidth of measurement, then $D^* \sim I_p/\sqrt{S(0)} \sim \eta g_p/\sqrt{g_n I_p}$ where $S(0) = I_{Bn}^2$. Hence, in background limited operation, the detectivity:

$$D_{Blip}^* \sim \sqrt{\eta \frac{g_p}{g_n}} = \sqrt{\eta(1-p_c)}\,. \tag{7}$$

Assuming constant photoionization efficiency, the background-limited detectivity increases with the decrease of capture probability. In general, the capture probability p_c and escape probability p_e can be related as p_c = 1- p_e, and hence if $p_e \rightarrow 1$, then $p_c \rightarrow 0$, and the detectivity is determined by the dark current noise. In this non-background limited condition, the total current is due to the dark current, and its magnitude is determined by the carrier concentration and drift velocity. Thus, in this case:

$$D_{dark}^* \sim \eta g_p/\sqrt{g_n} \cong \eta\sqrt{1/p_c}, \tag{8}$$

and the dark current limited detectivity also increases with decrease of capture probability, p_c.

Trapping of the carriers in the emitter/barriers leads to a significant charge buildup in the emitter/barriers and hence reduces the response. Grading the barrier, however, produces an offset between the barrier and emitter that reduces the recombination mechanism, and increases the gain owing to a higher momentum of the carriers[12, 19]. As shown in Figure 8 (b), and its inset, based on equation 5, a comparison of the dark current and photocurrent noise gains confirm that the escape probability of carriers is enhanced by grading the barrier, which results in further enhancement of specific detectivity (see equations 7 and 8). Increasing the emitter thickness for graded barriers then increases the response owing to increased absorption. At the same time, the escape probability of carriers' decreases with increasing emitter thickness[18] due to limited carrier life time. Hence, the dark current slightly decreases and the specific detectivity increases with increasing emitter thickness (Figure 9). At room temperature, even though the responsivity is low (≈ 8μA/W), a moderate specific detectivity (D*) ≈ 1.25x10^5 Jones for SP1007 was observed owing to the low noise spectral density, S (f*)*. To increases this further, the design of high performance device needs optimization for higher absorption, and lower dark current.

IV. Conclusion

In conclusion, the noise levels in p-type GaAs/AlGaAs heterostructures have been measured with both flat and graded barriers. At low temperature and low bias, the frequency independent G-R shot noise prevails whilst as temperature rises, both 1 /f and Johnson add to the shot noise. Comparisons of dark and photocurrent noise gains confirm that the escape probability of carriers is enhanced by grading

the barrier, whilst the graded barrier also reduces the recombination mechanism owing to the higher momentum of carriers. Despite only a very small change in noise density with increasing emitter thickness, the specific detectivity does increase significantly owing to higher absorption efficiency. Thus, optimizing the emitter thickness of graded barrier devices to enhance the absorption efficiency, and also increase the escape probability and lower dark current, enhances the specific detectivity of devices.

Acknowledgements

This work was supported in part by the U.S. Army Research Laboratory and the U. S. Army Research Office under contract/grant number W911NF-12-2-0035. We are also grateful for support from the UK's EPSRC (EP/E048811/1), the European Research Council program 'TOSCA' (247375), the Wolfson Foundation, and the Royal Society. Financial support provided by The Center for Diagnostics and Therapeutics of Georgia State University to S. Wolde as a Fellowship is also acknowledged.

References

1. V. Palenskis, J. Matukas, S. Pralgauskaitė, D. Seliuta, I. Kašalynas, L. Subačius, G. Valušis, S. P. Khanna and E. H. Linfield, J. of Appl. Phys. **113**, 083707 (2013).
2. F. N. Hooge, Phys. Lett. A **29**, 139 (1969).
3. F. N. Hooge and L. K. J. Vandamme, Phys. Lett. A **66**, 315 (1978).
4. H. Mikoshiba, IEEE Trans. on Electron Dev. **29**, 965 (1982).
5. A. Van Der Ziel, in *Advances in Electronics and Electron Physics*, edited by L. Marton and C. Marton (Academic Press, 1979), Vol. 49, pp. 225-297.
6. A. L. McWhorter, in *Semiconductor surface physics* (University of Pennsylvania Press 1957), pp. 207.
7. S. Kalem and G. E. Stillman, Jpn J. of Appl. Phys. **33**, 6086 (1994).
8. J. Szatkowski, E. Płaczek-Popko, K. Sierański and O. P. Hansen, J. of Appl. Phys. **86** (3), 1433 (1999).
9. J. Szatkowski, K. Sierański, A. Hajdusianek and E. Płaczek-Popko, Physica B: Condensed Matter **340**, 345 (2003).
10. C. Kayis, J. H. Leach, C. Y. Zhu, W. Mu, X. Li, U. Ozgur, H. Morkoc, X. Yang, V. Misra and P. H. Handel, Electron Dev. Lett. IEEE **31** (9), 1041 (2010).
11. A. G. U. Perera, S. G. Matsik, P. V. V. Jayaweera, K. Tennakone, H. C. Liu, M. Buchanan, G. Von Winckel, A. Stintz and S. Krishna, Appl. Phys. Lett. **89** (13), 131118 (2006).
12. P. K. D. D. P. Pitigala, Y. F. Lao, A. G. U. Perera, L. H. Li, E. H. Linfield and H. C. Liu, J. of Appl. Phys. **115** (6), 063105 (2014).
13. F. Pascal, S. Jarrix, C. Delseny, G. Lecoy and T. Kleinpenning, J. of Appl. Phys. **79**, 3046 (1996).
14. F. N. Hooge, T. G. M. Kleinpenning and L. K. J. Vandamme, Rep. on Prog. in Phys. **44**, 479 (1981).
15. Y. Paltiel, N. Snapi, A. Zussman and G. Jung, App. Phys. Lett. **87** (23), 231103 (2005).
16. H. C. Liu, Appl. Phys. Lett. **61** (22), 2703 (1992).
17. M. Ershov and H. C. Liu, J. of Appl. Phys. **86** (11), 6580 (1999).
18. D. G. Esaev, M. B. M. Rinzan, S. G. Matsik and A. G. U. Perera, J. of Appl. Phys. **96** (8), 4588 (2004).
19. S. G. Matsik, P. V. V. Jayaweera, A. G. U. Perera, K. K. Choi and P. Wijewarnasuriya, J. of Appl. Phys. **106** (6), 064503 (2009).

Table and table caption

Device No.	Lower edge (X_1)	Higher edge (X_2)	Constant barrier (X_3)	Emitter thickness (W)
SP1001	0.75	0.75	0.57	80 nm
SP1005	0.45	0.75	0.57	20 nm
SP1006	0.45	0.75	0.57	50 nm
SP1007	0.45	0.75	0.57	80 nm

Table1: Device structure details listing the different aluminum mole fractions (X_1, X_2, and X_3) used for the barriers, as illustrated in Figure 1. All emitters are p-doped at 1×10^{19} cm^{-3}.

Figures and figure captions

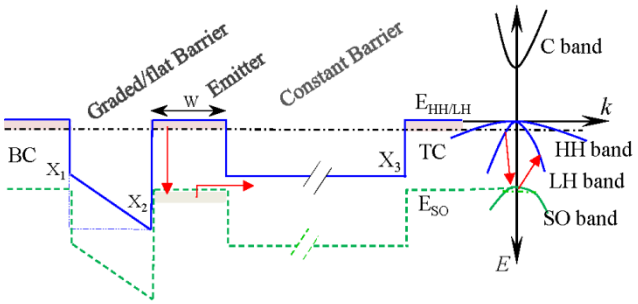

Fig. 1 Schematic diagram of the valence band structure at wave vector k = 0 and E–k diagram for an emitter region of the device: for the graded barrier structures $X_1 < X_2$ and in the constant barrier structure $X_1 = X_2$. The emitter thicknesses (W) and Al mole fractions (X_i) are tabulated in Table 1. The top contact (TC), bottom contact (BC), and the emitter are *p*-doped (10^{19} cm^{-3}). The dashed-dotted line represents the fermi level of heavy hole (HH)/light hole (LH) band. The dotted line represents split-off (SO) band in the device. The arrows indicate the possible transition mechanisms: a direct transition from LH to SO band followed by scattering back to LH band.

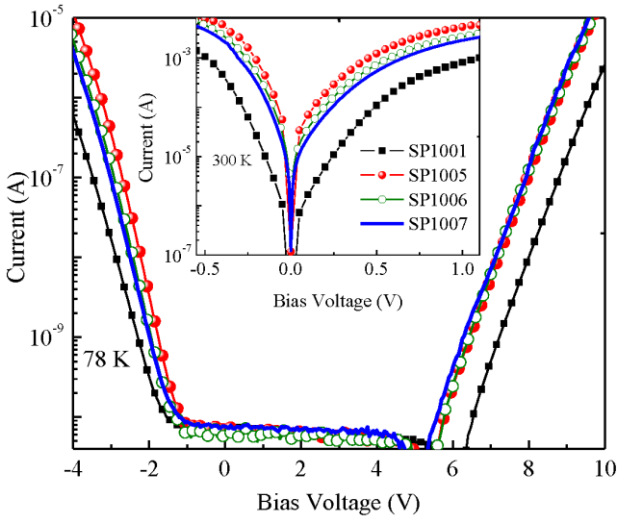

Fig. 2 (Color online) The dark IV characteristics of the four samples (SP1001 to SP1007) at 78 K and 300 K. The lowest dark current is observed in SP1001.

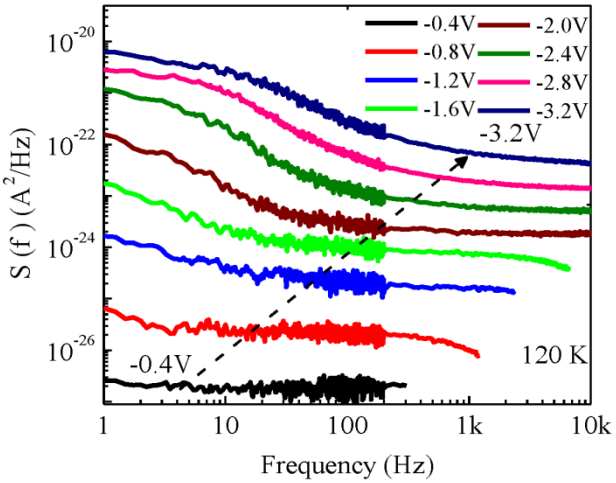

Fig. 3 (Color online) The noise power spectral density, S (*f*) at 120 K under different bias voltages for sample SP1005. At lower bias, the noise spectral density is independent of frequency.

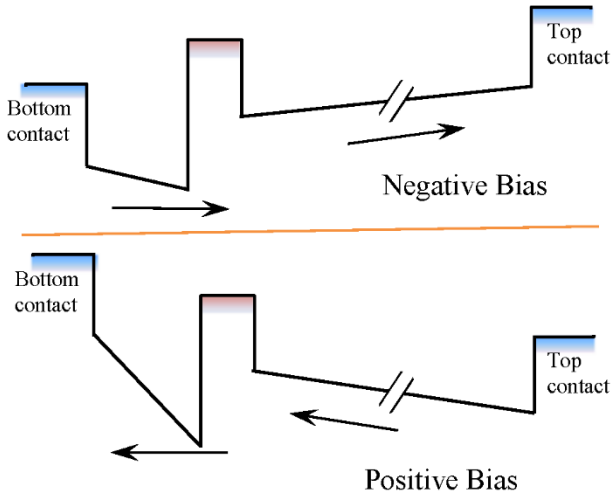

Fig. 4 (Color online) Graded barrier structure with energy band alignments under applied electric field.

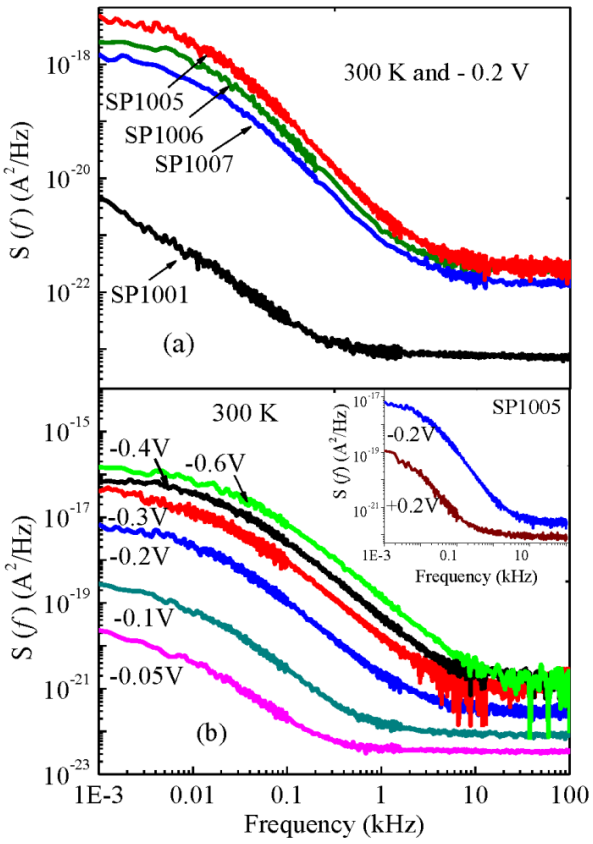

Fig. 5 (Color online) (a) The noise power spectral density (S (*f*)) of the wafers under a constant bias voltage of 200 mV. The device with flat barrier (SP1001) has the lowest noise spectral density. (b) The variation of noise power spectral density with bias for SP1005. Increasing biases shift the corner frequency toward higher frequencies. The inset shows the comparative noise power spectral density for positive and negative biases.

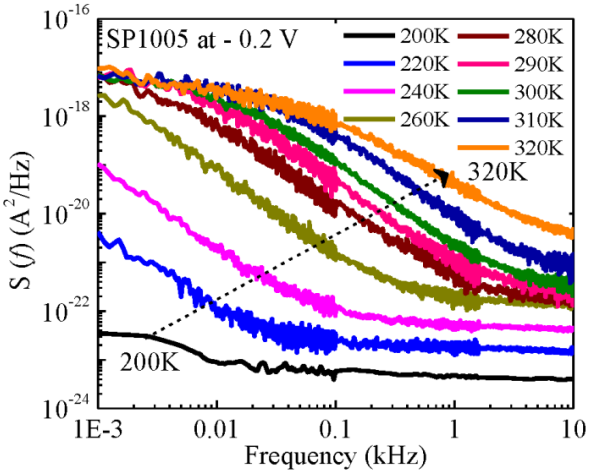

Fig. 6 (Color online) The noise current spectral density S (*f*) measured for a temperature range from 200 K to 320 K at a bias -0.20 V for SP1005. At higher temperatures, the G-R noise starts to appear.

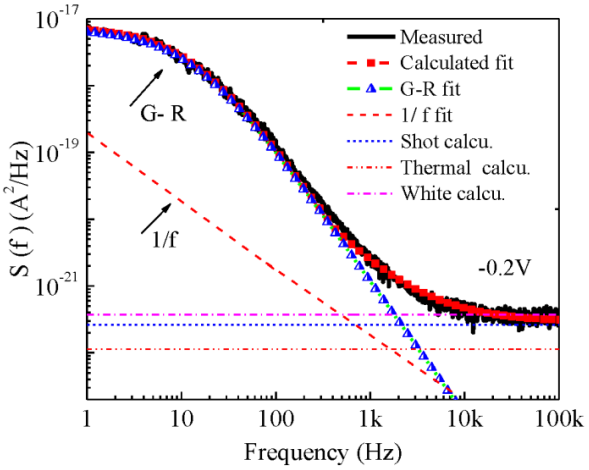

Fig. 7 (Color online) Experimentally measured noise spectra with theoretical and calculated fits for different components of noise. The white noise is the sum of shot and thermal noise.

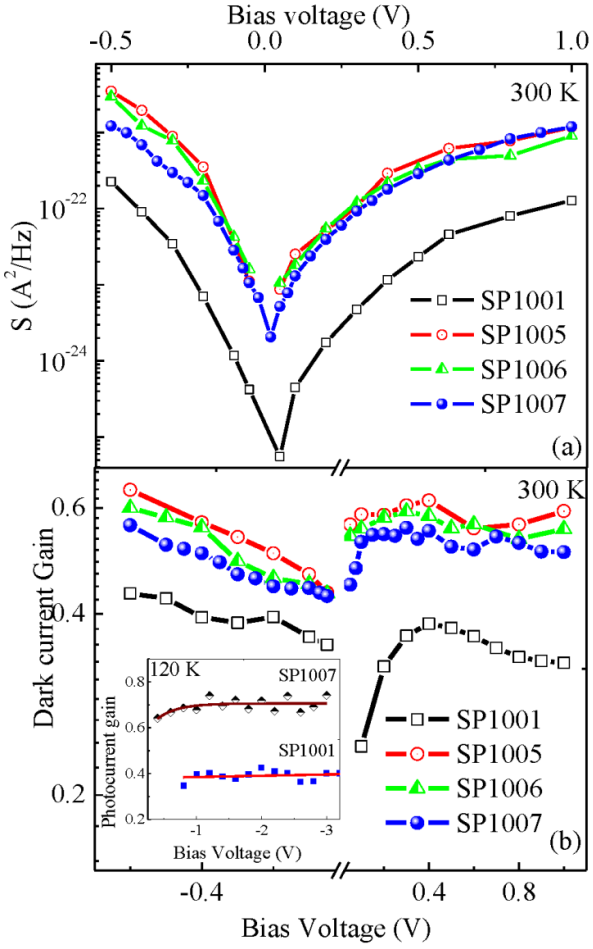

Fig. 8 (Color online) (a) A comparison between the measured noise power spectral densities for different structures at ~ 10 kHz. The device with constant barrier (SP1001) has the lowest noise power spectral density, and for graded structures there is hardly any change with different emitter thickness. (b) Comparison of dark current gains for the three different wafers. In the inset, solid lines are best fit to experimental data and show comparisons of photocurrent noise gain for flat and graded barrier heterojunctions at 120 K.

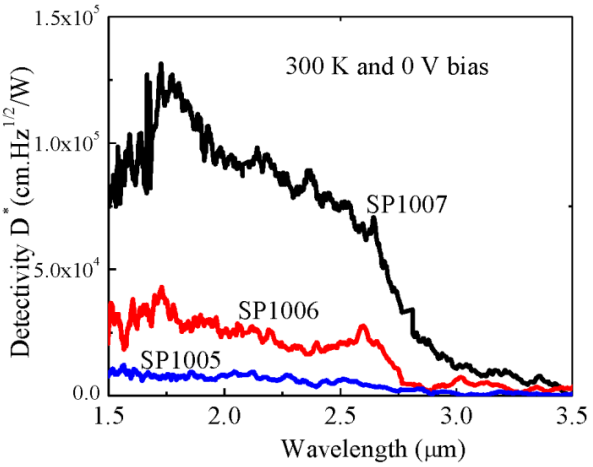

Fig. 9 (Color online) Comparison of detectivities for different emitter thickness (20 nm, 50 nm, and 80 nm). The thickest emitter (SP1007) has relatively the highest detectivity.